



RESEARCH ARTICLE OPEN ACCESS

Enzymatic Remodelling of Tumour Microenvironment Enhances Anti-CEACAM5 CAR T-Cell Efficacy Against Colorectal Cancer

Debasis Banik¹  | Christopher J. Ward² | Soura Chakraborty² | Ziwei Zhang¹ | Daniel Heraghty¹ | Prasanna Suresh¹ | Bing Li¹ | Shekhar Kedia¹ | Jhuma Pramanik² | Simon J. Davis^{3,4} | James P. Roy⁵ | Michael A. Chapman^{5,6,7} | Bidesh Mahata² | David Klenerman¹ 

¹Yusuf Hamied Department of Chemistry, University of Cambridge, Cambridge, UK | ²Department of Pathology, University of Cambridge, Cambridge, UK | ³Radcliffe Department of Medicine, John Radcliffe Hospital, University of Oxford, Oxford, UK | ⁴Medical Research Council Translational Immune Discovery Unit, John Radcliffe Hospital, University of Oxford, Oxford, UK | ⁵MRC Toxicology Unit, University of Cambridge, Cambridge, UK | ⁶Department of Haematology, University of Cambridge, Cambridge, UK | ⁷Addenbrooke's Hospital, Cambridge Universities Foundation Trust, Cambridge, UK

Correspondence: Debasis Banik (db920@cam.ac.uk) | Bidesh Mahata (bm562@cam.ac.uk) | David Klenerman (dk10012@cam.ac.uk)

Received: 28 May 2025 | **Revised:** 8 December 2025 | **Accepted:** 9 December 2025

Keywords: CAR T cell | CEACAM5 | CRC | enzyme | glycolyx

ABSTRACT

Chimeric antigen receptor (CAR) T-cell therapy has shown unprecedented success in haematological cancers but faces challenges in solid tumours. Although carcinoembryonic antigen-related cell adhesion molecule 5 (CEACAM5) is differentially expressed in many solid tumours, anti-CEACAM5 CAR T-cells are ineffective. Here, we have studied the interaction of CEACAM5 targeting primary CAR T-cells with colorectal cancer (CRC) cells using fluorescence microscopy. We found that CRC cells' glycolyx is much thicker than that of the CAR T cell causing delayed activation. Oscillating calcium fluxes, indicative of non-sustained CAR T cell activation, are observed when CAR T cells interacted with CRC cells, which increased with increasing cell-seeding time. Significant reduction in cytotoxicity is observed on going from early to longer-seeded CRC monolayers. Imaging revealed that this effect correlated with a progressive loss of accessible CEACAM5 antigen on the CRC cell surface, possibly due to their sequestration in the intercellular junction, rendering CAR T cell engagement less effective. Local proteolytic treatment with trypsin to disrupt the CRC cell monolayer, using a micropipette, increased CEACAM5 availability, decreased glycolyx thickness, and restored sustained CAR T cell calcium fluxes. Similar enhanced interaction is observed after treatment of CRC cell monolayer with hyaluronidase, approved for use in humans. Enzymatic treatment significantly enhanced CAR T cell-mediated cytotoxicity and increased the percentage of TNF- α -secreting CAR T cells. We observed limited availability of CEACAM5 on human colorectal cancer tissues, whereas treatment with trypsin or hyaluronidase increased accessibility. Our results reveal why CAR T cells targeting CEACAM5 are ineffective and suggest possible routes to improved therapy for CRC.

1 | Introduction

T cells are an essential part of the adaptive immune system. Each T cell expresses T-cell receptors (TCRs) which recognise peptide major histocompatibility complexes (pMHCs) on the

surface of antigen-presenting cells (APCs). In contrast, synthetically designed chimeric antigen receptors (CARs) originally comprised target-binding single-chain variable fragments (scFVs) of antibodies connected to an intracellular signaling domain, i.e., that of the CD3 ζ subunit of the TCR, via a transmembrane

This is an open access article under the terms of the [Creative Commons Attribution](https://creativecommons.org/licenses/by/4.0/) License, which permits use, distribution and reproduction in any medium, provided the original work is properly cited.

© 2026 The Author(s). *Advanced Science* published by Wiley-VCH GmbH

region. Additional signaling domains, i.e., from CD28 and 4-1BB contribute to later generations of CARs. Recently, CAR T-cell therapy has been approved by the United States Food and Drug Administration (FDA) for the treatment of B cell acute lymphoblastic leukemia (ALL), with several products now in use in the clinic [1–4]. However, the same therapy is ineffective in solid tumours, including colorectal cancer (CRC) [5–8]. CRC, the third most common global cancer, is responsible for ~10% of total cancer incidences and deaths in 2020, with ~30 months of median overall survival for metastatic CRC (mCRC) patients [9].

Understanding CAR T cell activity and limitations is essential for generating better therapies. CAR T cells require higher antigen concentrations than native T cells for activation [10]. Lack independent CAR T cell activation was shown to be driven by the CD28 signaling domain and the SRC family kinase Fyn [11, 12], leading to the formation of a non-classical and potent immunological synapse generating rapid cytotoxicity [13]. Recently, Xiao et al. showed that the exclusion of the large phosphatase CD45 at the anti-CD19 CAR T-cell/Raji B cell interface, used as a model system, is intrinsic to CAR T cell activation, likely due to the phosphatase exclusion favouring net CAR phosphorylation by kinases, as proposed by the ‘kinetic-segregation’ (KS) model [14, 15].

Carcinoembryonic antigen-related cell adhesion molecule 5 (CEACAM5) is overexpressed in many cancer types including lung, breast (luminal A & B), pancreatic tumours, and CRC. A recent study comparing multiple anti-CEACAM5 scFvs (M5A, hMN-14, BW431/26, and C2-45) demonstrated that whilst scFv affinity and stability influence CAR T-cell phenotype and function, the target tumour context and antigen density remain critical determinants of therapeutic efficacy [16]. It was found that M5A, hMN-14, and BW431/26 CAR T cells all exhibited effective tumour cell lysis and IFN- γ release when co-cultured with CEACAM5-positive tumour cells in vitro, with differences primarily attributed to CEA expression levels rather than fundamental differences in scFv recognition [16]. Du-San Baek and colleagues [17, 18] developed a fully human anti-CEACAM5 monoclonal antibody (1G9) targeting the membrane-proximal A3B3 domains. The IgG1 form of 1G9 demonstrated CEACAM5-specific antibody-dependent cellular cytotoxicity (ADCC) against prostate cancer cells both in vitro and in vivo, whilst 1G9-based CAR T cells showed potent antitumour activity in a prostate cancer mouse model, indicating therapeutic potential for CEACAM5-positive neuroendocrine prostate cancer and other malignancies. Despite promising preclinical results, there has been little progress treating tumours with CAR T cells for multiple reasons, such as the variation in the tumour microenvironment, poor accessibility of the cancer cells to the CAR T cells, poor persistence of the CAR T cells, and respiratory toxicity [19].

Here, we investigate the interaction of anti-CEACAM5 CAR T-cells with CEACAM5⁺ CRC cell lines in vitro and with advanced model bilayers, using imaging methods, established previously [20]. We observed tumour microenvironment barriers, including CEACAM5 sequestration and the thick glycocalyx of CRC cell play crucial roles in reducing the effectiveness of CAR T-cell/CRC cell interactions. We also observed enhanced interaction, increased killing of CRC cells, and a higher percentage of TNF- α -secreting CAR T cells when we locally treated the CRC cell monolayers with a proteolytic enzyme,

trypsin, or glycocalyx-degrading enzyme, hyaluronidase. CEACAM5 was also concealed in human colorectal cancer tissues, but increased availability was observed following treatment with either trypsin or hyaluronidase. Our results suggest routes to improved immunotherapy of CRC with hyaluronidase/CAR T-cells.

2 | Results

2.1 | Impaired Activation and Decreased Anti-CEACAM5 CAR T-Cell-Mediated Cytotoxicity in Colorectal Cancer Models

Jurkat and primary human T-cell-derived anti-CEACAM5 CAR T-cells were prepared from clone hMN-14 which binds to the A3B3 domain of CEACAM5 (Figure S1A–F) [21, 22]. CEACAM5[−] (RKO as control) and CEACAM5⁺ (LS-174T & LS-1034) CRC cells were used in our experiment (Figure S1G–I). To establish baseline CAR T-cell functionality, we first validated anti-CEACAM5 Jurkat CAR T-cells on our “second generation” supported lipid-bilayer system (SLB2), which presents ligands for the small and large adhesion proteins CD2 (i.e., CD58) and LFA-1 (i.e., ICAM-1), alongside the major antigen presenting cell (APC) glycocalyx elements, CD43 and CD45 (~40 nm in length), human CEACAM5/CD66e protein as an antigen for the CAR T-cell, and gp100-MHC, an irrelevant peptide-MHC used to block free nickellated lipids.

We prepared CEACAM5 positive (CEACAM5⁺) and CEACAM5 negative (CEACAM5[−]) SLB2s. CAR T-cells labelled with Fluo-4-AM (a calcium indicator) and CellMask Deep Red (a plasma membrane stain) were then allowed to interact with the SLB2s. We observed that CAR T-cells formed close contacts by excluding CD45/CD43 on the bilayer and produced robust calcium fluxes on the CEACAM5⁺ SLB2s (Movie S1). On CEACAM5[−] (control) SLB2s, transient interactions and no calcium fluxes were observed (Figure S2A and Movie S1). This result shows that CAR T-cells are highly sensitive to the presence of human CEACAM5 protein. Interestingly, we observed ~40% average exclusion of CD45/CD43 by CAR T-cells (Figure S2B), similar to wild-type Jurkat and primary T-cells in our previous study [20], suggesting similar interactions with the SLB2 system.

Figure 1 shows early-stage imaging of the anti-CEACAM5 CAR T-cell/CRC cell interaction using brightfield and epifluorescence calcium imaging. We sought to mimic tumour growth-related changes by plating out CRC cells for 24 and 48 h. Figure 1A shows the experimental scheme for the cell-cell assay wherein Fluo-4-AM pre-labelled CAR T-cells interact with the LS-174T monolayer and produce calcium fluxes. Noting the off-target respiratory distress experienced by colon cancer patients within 15 min of CAR T-cell infusion [23], we decided to focus on the first 1 h of CAR T-cell/LS-174T interaction using simultaneous measurement of calcium fluxes and brightfield images.

Firstly, we monitored the interaction using a 20X objective lens and found that the Jurkat CAR T-cells produced sustained calcium fluxes (red arrows in Movie S2) with early-seeded LS-174T monolayer (24 h), whereas, no sustained flux was observed following longer seeding of the monolayers (48 h). The triggering

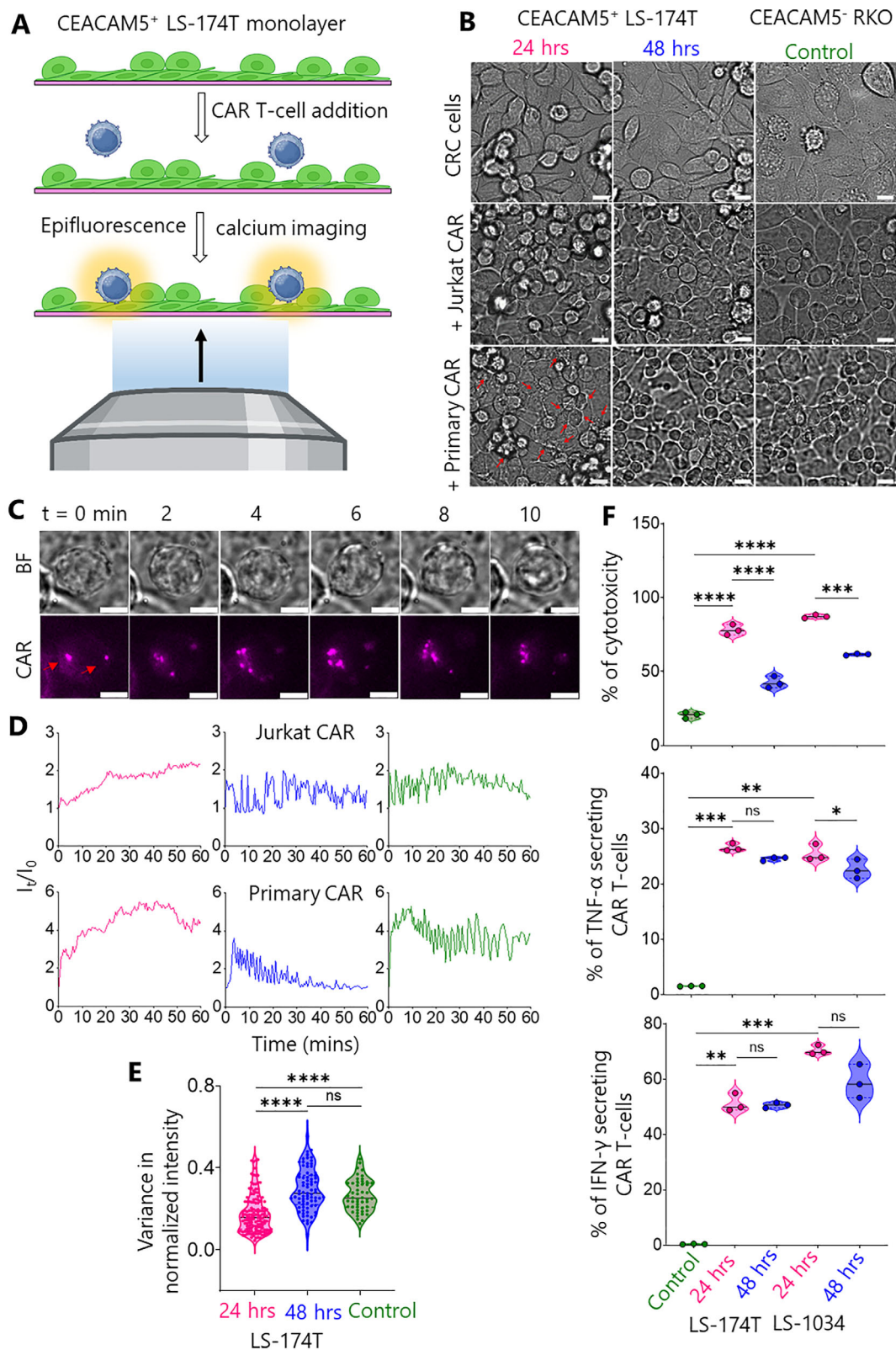


FIGURE 1 | CAR T-cell/CRC cell interaction. (A) Cartoon shows CAR T-cells interacting with CEACAM5⁺ LS-174T cell monolayer. Live T-cell/tumor interaction was monitored using epifluorescence calcium and brightfield imaging. (B) Brightfield images show differently seeded LS-174T (pink, blue: 24 and 48 h, respectively) and CEACAM5⁻ RKO monolayers (olive: 24 h) interacting with Jurkat and primary CAR T-cells. Red arrows indicate killing of LS-174T cells by primary CAR T-cells. Scale bars are 10 μ m. The same colour code will be used hereafter throughout all figures. (C) Time-series showing CAR accumulation (red arrows) while Jurkat CAR T-cells interacting with 24 h seeded LS-174T monolayer. Scale bars are 5 μ m. (D) Representative epifluorescence calcium flux colour coded traces of Jurkat and primary CAR T-cells while interacting with LS-174T and RKO monolayers. (E) Violin plots show variance in normalized calcium flux intensity of CAR T-cells on CRC cell monolayers. Data shown in D & E were pooled from 6

of CAR T-cells was substantially delayed on early-seeded LS-174T monolayers compared to the SLB2 (peak activation longer than 1 h vs. within 3 min in Figure S2C). We repeated the same experiment with LS-1034, a second CEACAM5^{high} CRC cell line, and found almost no T-cell triggering, even for the early seeding condition (Movie S3).

To investigate signaling on LS-174T monolayers in more details, we used a 60X objective lens. Brightfield images of LS-174T and the RKO monolayer (24 h) interacting with Jurkat CAR T-cells are shown in Figure 1B. CAR accumulation was observed as bright puncta formation during interaction with the early-seeded LS-174T monolayer (Figure 1C). Representative calcium flux traces are shown in Figure 1D and Movies S4 and S5. The increased and sustained calcium flux changed to oscillatory fluxes with increasing seeding time. Interestingly, similar oscillatory calcium fluxes were also observed on the RKO monolayer, suggesting that at the later seeding time-points there is very little antigen recognition. Figure 1B (third row, red arrows) and Movie S6 reveal extensive killing of the early-seeded LS-174T cells by primary CAR T-cells. In contrast, within the first 1 h of monitoring, no killing was observed for longer-seeded LS-174T and control monolayers. We present more calcium flux data Movies S7 and S8 to support our observations. We determined the variance of calcium flux fluctuations (Figure 1E). The variance in the normalised calcium flux fluctuations was substantially lower for T-cells interacting with the early- versus the longer-seeded LS-174T and control monolayers. This result confirmed that significant increases in calcium flux oscillation accompany the early- to longer-seeded LS-174T transition, with the latter condition being very similar to the control monolayer.

To confirm CAR T-cell-mediated killing of CEACAM5⁺ targets (LS-174T and LS-1034), we have performed cytotoxicity and cytokine release assays. Cytotoxicity was measured using lactate dehydrogenase (LDH) release and annexin V/propidium iodide (PI) assays (Figure 1F and Figure S2D and S1J), whilst cytokine secretion was quantified by intracellular cytokine staining and flow cytometry (Figure 1F). Cytotoxicity assays demonstrated significantly higher killing of CEACAM5⁺ LS-174T (~80%) and LS-1034 (~90%) cells compared to CEACAM5⁻ RKO cells (~20%), confirming antigen-specific cytotoxicity (Figure 1F). Interestingly, a time-dependent reduction in efficacy was observed, with cytotoxicity against CEACAM5⁺ cells declining significantly in longer-seeded monolayers compared to early-seeded conditions, from ~80% to ~40% for LS-174T and from ~90% to ~60% for LS-1034 (Figure 1F). Cytokine release assays showed significantly increased percentages of TNF- α - and IFN- γ -secreting CAR T cells when co-cultured with CEACAM5⁺ LS-174T and LS-1034 cells compared to CEACAM5⁻ RKO cells, further confirming antigen-specific T-cell activation (Figure 1F).

In summary, whereas anti-CEACAM5 CAR T-cells responded to early-seeded CRC cell monolayers, decreased activation and cyto-

toxicity was observed with increasing seeding time. Therefore, consistent with clinical observations [19], our results show that anti-CEACAM5 CAR T-cells respond poorly to CRC.

2.2 | The Thickened Glycocalyx of Colorectal Cancer Cells Creates a Significant Physical Barrier to CAR T Cell Engagement

The glycocalyx is a critical surface coating on the surface of all cells that modulates cell-cell interactions and can influence immune surveillance. The glycocalyx comprises dense arrays of negatively charged, heavily glycosylated proteins and polysaccharides, that forms a physical barrier to cell contact [24]. In cancer cells the glycocalyx increases in depth, making it more difficult for T-cells to kill cancerous cells, especially solid tumours [25, 26]. Therefore, it was of interest to test whether the decreased CAR T-cell/LS-174T interaction is associated with the presence of a thick glycocalyx on the tumour cell.

To measure the glycocalyx, CAR T-cells and early- and longer-seeded LS-174T cells were fixed and labelled with HMSiR-conjugated wheat germ agglutinin (WGA-HMSiR). WGA binds to the N-acetylglucosamine residues of the glycocalyx. We measured the glycocalyx thickness using resPAINT super-resolution (SR) imaging [27]. Figure 2A–C show 2D SR images of T-cell and LS-174T glycocalyxes, which are ~100 and ~400 nm thick, respectively. Figure 2D shows stimulated emission depletion (STED) image of LS-1034 cell glycocalyx with ~400 nm median glycocalyx thickness. Figure 2E confirms that the LS-174T and LS-1034 cell glycocalyx is significantly thicker than that of the CAR T-cells.

Interestingly, no significant variation in glycocalyx thickness was observed between early- and longer-seeded LS-174T cells (Figure 2E), indicating that the differential CAR T cell reactivity observed between these conditions cannot be attributed to changes in glycocalyx dimensions alone. This suggests that while the substantial glycocalyx disparity represents a physical barrier to effective CAR T cell engagement with tumour cells, additional factors likely contribute to the seeding-dependent differences in CAR T cell activation and cytotoxicity.

These findings establish that the glycocalyx of CRC cells creates a formidable spatial barrier that must be overcome for effective immunotherapeutic targeting, providing insight into possible mechanism underlying the limited efficacy of CAR T cell therapy against solid tumours.

2.3 | CEACAM5 sequestration at Tumour Cell–Cell Junctions Mediates Immune Evasion from CAR T Cell Recognition

To explore the reasons for the decrease in CAR T-cell/LS-174T reactivity with increasing seeding time, we performed

to 7 and 3 to 4 independent experiments of Jurkat CAR T-cell/CRC cell and primary CAR T-cell/CRC cell interactions, respectively with $n = 145$ (24 h), 77 (48 h), and 50 (Control). (F) Violin plots show primary CAR T-cell-induced cytotoxicity (LDH release, top) and cytokine release (middle, bottom) against CEACAM5⁺ targets (LS-174T, LS-1034) compared with RKO control. The black lines in (E) and (F) indicate the median which were compared using two-sided Student's *t*-test. ns not significant, * $p \leq 0.05$, ** $p \leq 0.001$, *** $p = 0.0002$, **** $p < 0.0001$.

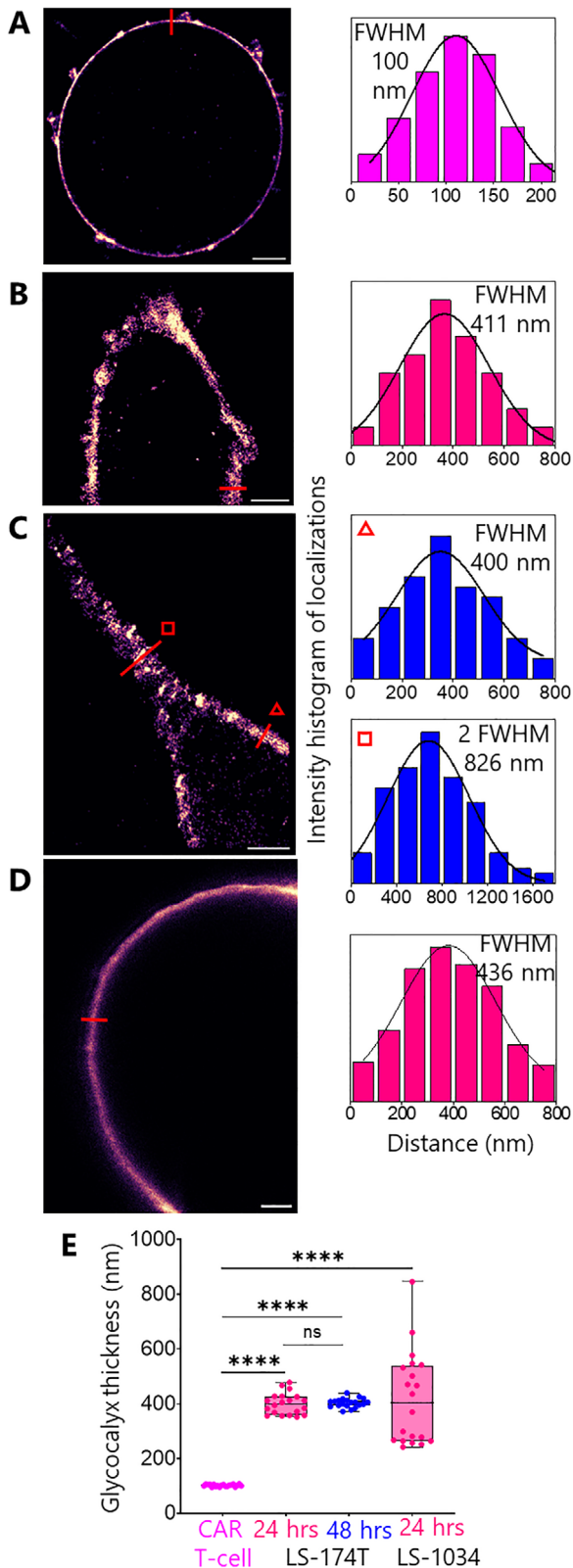


FIGURE 2 | Super-resolution (resPAINT & STED) (27) images of the glycocalyx. Representative 2D images of (A) CAR T-cell, (B-C) LS-174T cell (24 and 48 h seeded, respectively) and (D) LS-1034 cell glycocalyxes labelled with WGA-HMSiR (A-C; resPAINT) and WGA-Star Red (D; STED), respectively. Scale bars are 2 μm . Colour coded line plots as indicated in A-C (400 nm width) and D are shown in front of images. Colour code for T-cell is magenta. Glycocalyx thickness is shown at two

antigen mapping on the LS-174T monolayer using fluorescently labelled anti-CEACAM5 antibody. Strikingly, CEACAM5 distribution on LS-174T cells exhibited a temporal pattern of sequestration. In minimally established cultures (4 h post-seeding), CEACAM5 was abundantly available across the entire cell surface (Figure 3A, top row). On early-seeded monolayer, CEACAM5 redistributed predominantly to intercellular junctions with heterogeneous expression (Figure 3A, second row), a pattern commonly observed for solid tumour antigens. Notably, in longer-seeded monolayers, CEACAM5 became increasingly inaccessible, with staining patterns resembling the CEACAM5-negative RKO controls (Figure 3A, third and fourth rows). Quantitative analysis confirmed significant reduction in CEACAM5 accessibility on transitioning from early to longer-seeded LS-174T monolayers and the latter one showed no significant difference to RKO (Figure 3B). CEACAM5 sequestration was also observed in LS-1034 and in the CEACAM5⁺ lung cancer cell line A549 (Figure S3A,B).

This progressive antigen sequestration correlated with functional impairment, as evidenced by significantly increased T cell motility and track straightness on longer-seeded LS-174T monolayers compared to early-seeded cultures (Figure S3C-F and Movie S9). To determine whether this sequestration phenotype was antigen-specific or a general characteristic of CRC cells, we examined the distribution of two additional clinically relevant antigens. We engineered CD19-expressing LS-174T cells (Figure S3G,H) and examined endogenous HER2 expression. In contrast to CEACAM5, both CD19 and HER2 maintained homogeneous cell-surface distribution regardless of seeding duration (Figure 3A, bottom rows; Figure S3J,K). Furthermore, anti-CD19 CAR T-cells exhibited robust calcium signalling against longer-seeded CD19⁺ LS-174T monolayers (Figure S3I), confirming that CEACAM5 sequestration represents a distinctive immune evasion mechanism rather than a general feature of antigen presentation in maturing CRC cultures.

To characterize the functional consequences of CEACAM5 accessibility, we monitored primary CAR T cell interactions with early-seeded LS-174T monolayers using simultaneous calcium and lysosomal imaging. By labeling T-cells with Fluo-4-AM and lysotracker red, we observed calcium fluxes (~ 15 min after CAR T addition) preceding the recruitment of granules (~ 40 – 50 min) at the immunological synapse formed by the CAR T-cells with LS-174T cells (Figure 3C and Movie S10). We analysed the recruitment trajectories of the granules (Figure 3D and Movie S11) and found the mean speed of recruitment varies between 0.005 and 0.04 $\mu\text{m}/\text{sec}$. Davenport et al. did similar analyses of primary CAR T-cells targeting HER2 and found granule recruitment speeds of ~ 0.10 $\mu\text{m}/\text{sec}$ [13]. This

locations of C (triangle and square indicate 1*glycocalyx and 2*glycocalyx, respectively). Glycocalyx thickness was determined as the FWHM of the Gaussian fit. (E) Boxplot shows the glycocalyx thickness of CAR T-cell vs. LS-174T and LS-1034 cells. In each case, data points ($n = 20$) were extracted by measuring thickness at multiple locations of three individual images collected from three independent experiments. Medians were compared using two-sided Student's *t*-test. ns not significant, **** $p < 0.0001$.

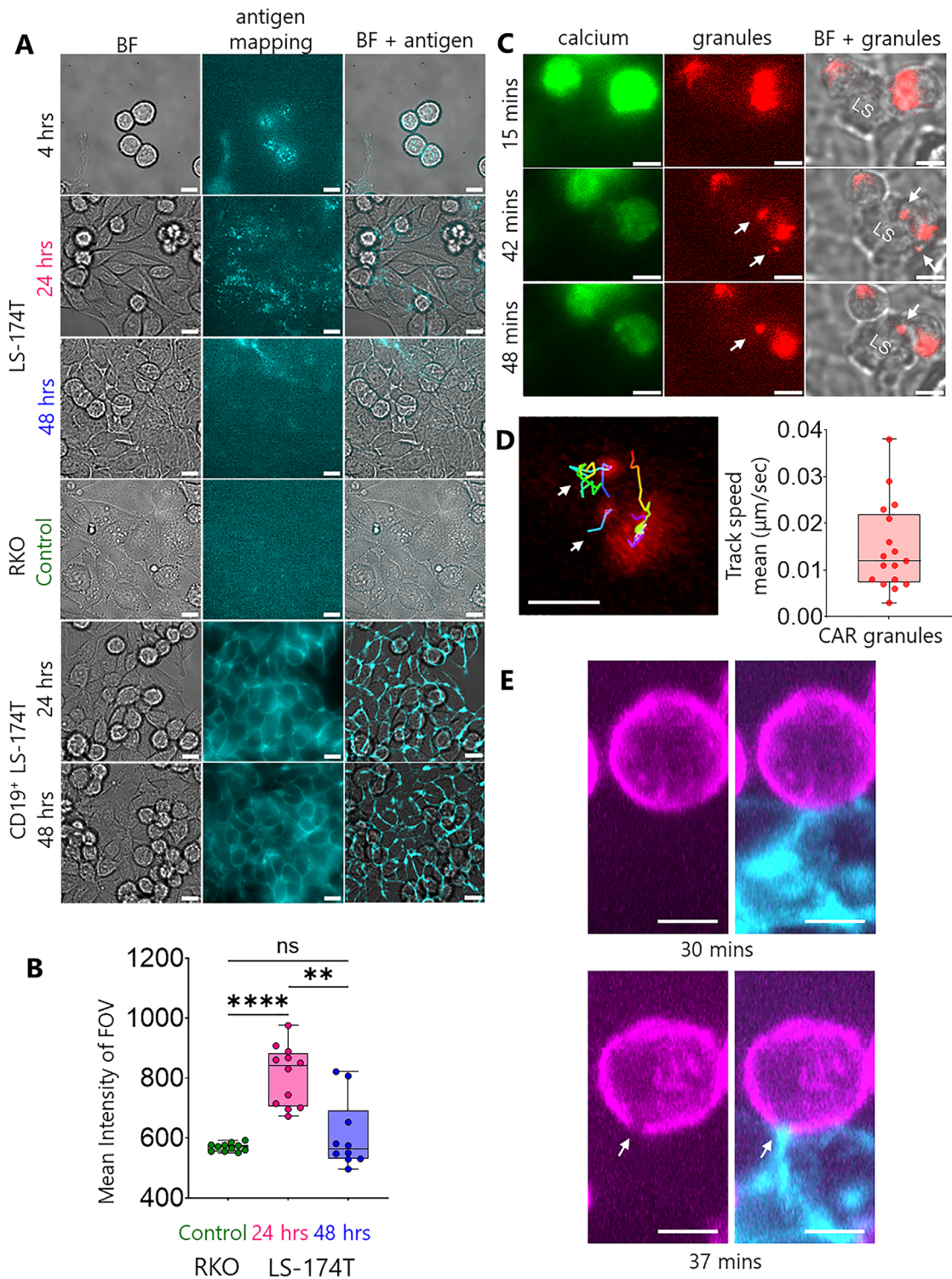


FIGURE 3 | Antigen mapping, granules recruitment and CD45 exclusion while CAR T-cell/CRC cell interaction. (A) Middle column shows CEACAM5 and CD19 mapping on LS-174T, RKO and CD19⁺ LS-174T cells/monolayers, respectively at different seeded conditions mentioned on the left. The left and right columns show brightfield (BF) and merged (brightfield and antigen) images, respectively. For each seeding condition, images are representative of $n = 10$ –15 FOVs. (B) Quantification of mean CEACAM5 intensity of FOV for 24 h ($n = 12$), 48 h seeded ($n = 10$) LS-174T and RKO ($n = 11$) monolayers. Medians were compared using two-sided Student's t -test. **** $p < 0.0001$, ** $p = 0.0054$, ns not significant. (C) Time series of calcium flux (left column) and granules recruitment (white arrows in middle and right columns) images show the sequence of events during primary CAR T-cell/LS174T cell (24 h seeded) interaction. Results are representative of $n = 9$ events collected from three individual FOVs. (D) Tracks (white arrows) and track speed mean (boxplot) of CAR granules. (E) Jurkat CAR T-cell (magenta)/LS-174T cell (cyan) conjugates at 30 and 37 min after mixing. CD45 exclusion (white arrows) at cell/cell interface was captured using epifluorescence selective plane illumination microscopy (eSPIM) and representative of $n = 12$ FOVs. Scale bars are 10 and 5 μm in A, C, D and E, respectively.

implies that granule recruitment speed is target-antigen dependent.

After observing CD45/CD43 exclusion on the SLB2 (Movie S1), we sought to image the same phenomenon at the CAR T-cell/tumour cell interface. Early-seeded LS-174T monolayers and Jurkat CAR T-cells were labelled separately with anti-epithelial cell adhesion molecule (EpCAM) antibody-Alexa 647 and Gap8.3-Alexa 488 (anti-CD45 antibody) conjugates, respectively, and then allowed to interact for 30 min. Figure 3E shows late-stage CD45 exclusion on T-cells (white arrows) at the CAR T-cell/LS-174T interface using a home-built epifluorescence selective plane illumination microscope (eSPIM).

2.4 | Enzymatic Remodelling of the Tumour Cell Intercellular Junctions Increases CEACAM5 Accessibility and Enhances CAR T Cell Function

The ineffectiveness of CEACAM5-targeting CAR T cells against CRC may be attributed to two key barriers we identified: antigen sequestration at intercellular junctions (Figure 3A,B and Figure S4A,B) and the thick glycocalyx of CRC cells (Figure 2). To address these limitations, we conceived the idea of treating longer-seeded LS-174T monolayers with the dissociating enzyme trypsin to re-expose the CEACAM5 and reduce the physical barrier of the glycocalyx.

To address CEACAM5 sequestration at intercellular junctions, we developed a localised trypsin delivery system using a micropipette (Figure 4A). This approach selectively disrupted cell-cell adhesions in the upper layer of longer-seeded LS-174T monolayers without compromising monolayer integrity (Movie S12). Calcium flux analysis revealed sustained signaling in anti-CEACAM5 CAR T-cells interacting with trypsin-treated LS-174T monolayers, mirroring responses observed in early-seeded cultures (Figure 4B and Movies S13 and S14). Control experiments using CEACAM5-negative RKO monolayers showed unchanged oscillatory calcium fluxes (Figure 4B), confirming treatment specificity. Variance analysis demonstrated significant reduction in calcium flux oscillations after trypsin treatment, comparable to early-seeded conditions (Figure 4C).

Immunofluorescence mapping revealed rapid CEACAM5 re-availability at the intercellular junction within 20 min post-trypsin application, to the extent observed for the early-seeded condition (Figure 4D). Super-resolution resPAINT imaging showed significant reduction of glycocalyx thickness to ~150 nm in the presence of trypsin, while creating discontinuous glycocalyx patches (Figure 4E).

We tested trypsin treatment on early-seeded LS-174T monolayers and observed faster triggering of Jurkat CAR T-cells measured as calcium fluxes, versus the untreated condition (Figure S2C). CEACAM5 mapping showed increased availability after treatment (Figure S4C).

This dual mechanism, antigen re-availability and glycocalyx thinning, explained restored CAR T cell activation kinetics, with primary CAR T-cells achieving target cell killing within 1 h on treated monolayers versus no cytotoxicity in controls (Movie S15).

2.5 | Hyaluronidase Pretreatment Overcomes Glycocalyx-Mediated Resistance to Anti-CEACAM5 CAR T- Cells

We investigated whether the improved CAR T-cell/LS-174T interaction is also observed when we apply glycocalyx-specific enzyme to reduce/remove the thickness or density of the glycocalyx of LS-174T cells. Hyaluronidase degrades hyaluronic acid [28], a component of the glycocalyx. We treated longer-seeded LS-174T monolayers with 25 U/mL hyaluronidase and observed sustained increased calcium flux of Jurkat CAR T-cells (Figure 4B). Figure 4C shows significantly decreased calcium flux fluctuations of CAR T-cells interacting with hyaluronidase-treated LS-174T monolayer comparable to the trypsin-treated condition. A similar result was observed following treatment with 0.5 U/mL heparinase, another glycocalyx-degrading enzyme (Figure S4D).

To determine whether enzymatic remodelling affects CD19 accessibility, CD19 expression was measured on longer-seeded CD19⁺ LS-174T monolayers, both untreated and after hyaluronidase treatment. Quantitative analysis confirmed that CD19 expression remained comparable between untreated and treated condition (Figure S4E). When Fluo-4-AM pre-labelled anti-CD19 CAR T cells were added to the enzyme-treated monolayer, a rapid calcium flux response was observed, consistent with that seen under untreated condition previously (Figure S4E vs. S3I).

To directly demonstrate that enzymatic remodelling enhances CAR T-cell-mediated killing, we have performed cytotoxicity and cytokine release assays on trypsin- and hyaluronidase-treated longer-seeded tumour cell monolayers (Figure 4F and Figure S4F). Treatment with trypsin or hyaluronidase significantly increased CAR T-cell-mediated killing compared to untreated monolayers. Cytotoxicity increased from ~40% (untreated) to ~52% (hyaluronidase-treated) in LS-174T cells and from ~60% (untreated) to ~70% (trypsin-treated) in LS-1034 cells (Figure 4F). Interestingly, using the annexin V/propidium iodide (PI) assay, a significantly increased dead cell population, not due to the apoptotic pathway, was observed following enzymatic treatment (Figure S4F). A significant increase in the percentage of TNF- α -secreting CAR T cells was observed on LS-174T and LS-1034 monolayers following hyaluronidase treatment (Figure 4F). Whilst trypsin and hyaluronidase treatment showed a trend toward increased IFN- γ -secreting CAR T cells, the differences did not reach statistical significance, likely due to the inherent variability in IFN- γ measurements (Figure 4F). Overall, these findings corroborate the sustained calcium flux responses observed in enzymatically treated monolayers and confirm that removing the glycocalyx barrier directly enhances CAR T-cell activation and cytotoxic function.

2.6 | Hyaluronidase-Mediated Glycocalyx Degradation Unmasks CEACAM5 in Human Colorectal Cancer Tissue

To determine whether the limited efficacy of anti-CEACAM5 CAR T-cell therapy in CRC patients is due to restricted antigen accessibility, we assessed CEACAM5 availability in human CRC tissue sections before and after enzymatic treatment. Immunofluorescence staining of untreated

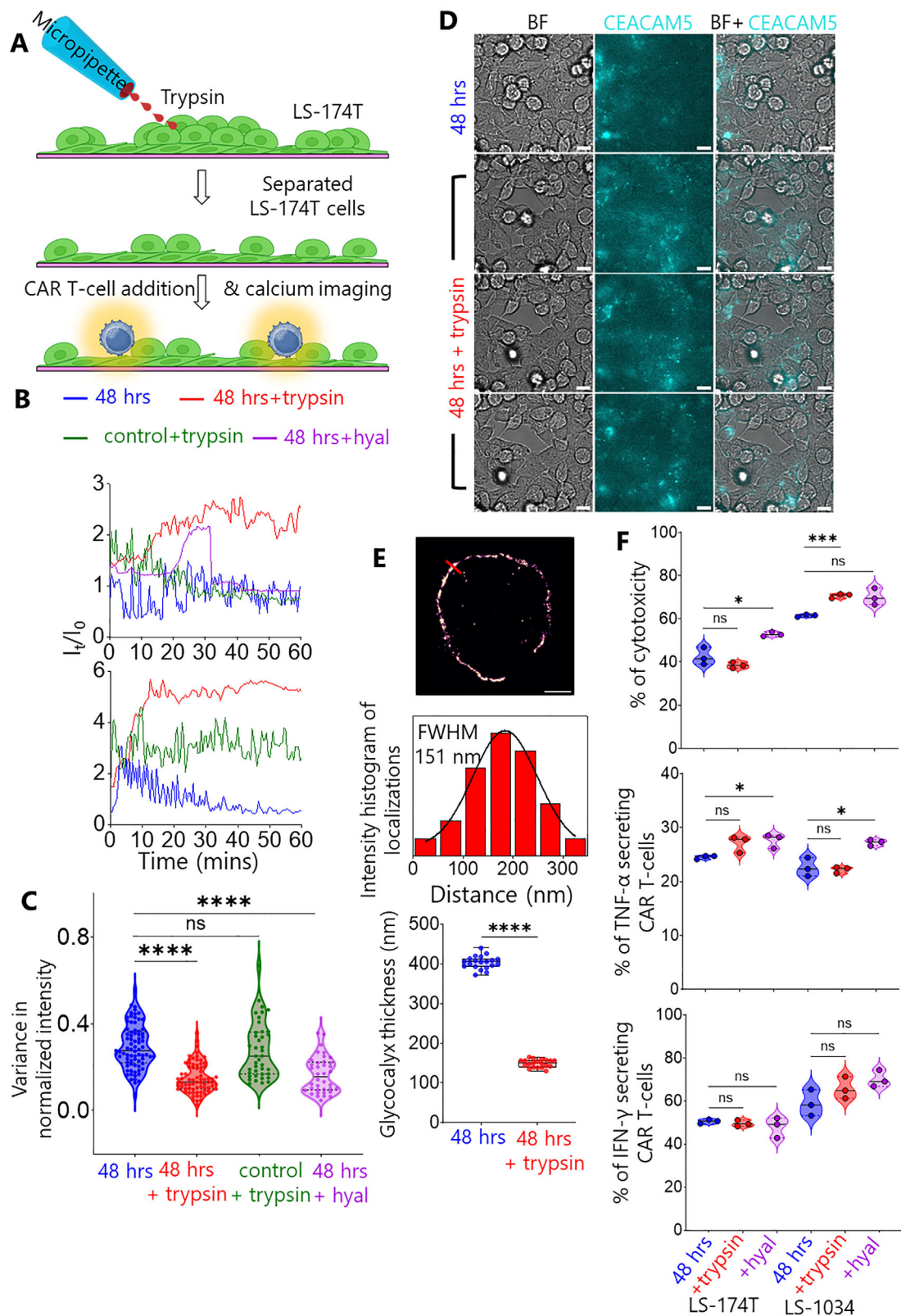


FIGURE 4 | Trypsin and hyaluronidase (hyal) treatment to improve CAR T-cell/CRC cell interaction. (A) Cartoon shows trypsin treatment on 48 h seeded LS-174T monolayer using a micropipette to dissociate cells followed by CAR T-cell addition and epifluorescence calcium imaging. (B) Calcium flux traces of CAR T-cells before (48 h), after trypsin (48 h + trypsin, red) and hyaluronidase (48 h + hyal, purple) treatment on LS-174T monolayer, and after trypsin treatment on RKO (olive) monolayers. The y-axis of the graphs are shifted from 1 for better comparison. Top and bottom graphs indicate Jurkat CAR and Primary CAR, respectively. (C) Violin plot shows comparison of variance in normalized calcium flux intensity of CAR T-cells on CRC cell monolayers before and after trypsin and hyaluronidase treatments with $n = 77$ (48 h), 74 (48 h + trypsin on LS-174T), 41 (48 h + trypsin on RKO) and $n = 28$ (48 h + 25 U/mL hyaluronidase on LS-174T). (D) CEACAM5 mapping (middle row) on LS-174T monolayer before and after trypsin treatment.

CRC tissue from multiple patients ($n = 13$) revealed that CEACAM5 was largely inaccessible, with only sparse and heterogeneous surface expression observed across tumour regions (Figure 5A, untreated). Control experiments using secondary antibody alone confirmed the specificity of the CEACAM5 signal and established the baseline for detection (Figure S5A).

Upon treatment with hyaluronidase (75 U/mL), a marked increase in CEACAM5 accessibility was observed. Quantitative analysis across multiple fields of view demonstrated a significant 2- to 5-fold elevation in mean CEACAM5 fluorescence intensity following hyaluronidase treatment compared to untreated controls (Figure 5B). This effect was consistent in 4 patient samples, indicating that hyaluronidase-mediated degradation of the tumour glycocalyx efficiently unmaskes sequestered CEACAM5 epitopes. Dose titration experiments established 75 U/mL as the optimal concentration for maximal antigen exposure without overt tissue disruption (Figure 5B).

For comparison, trypsin treatment (0.0005%) also substantially increased CEACAM5 accessibility, with some tissues exhibiting up to a 12-fold enhancement (Figure 5B). However, a subset of patient samples did not respond to trypsin enzymatic treatment, which was attributed to either intrinsic CEACAM5-negativity or preserved epithelial architecture indicative of early-stage disease (Figure S5B).

Collectively, these results demonstrate that the dense glycocalyx in human CRC tissues acts as a physical barrier, concealing CEACAM5 from CAR T-cell therapeutic recognition. Hyaluronidase treatment effectively degrades this barrier, revealing previously hidden CEACAM5 and supporting the rationale for combining glycocalyx-targeting strategies with CAR T-cell therapy to improve immunotherapeutic targeting of solid tumours.

3 | Discussion

CAR T-cell therapy has revolutionised treatment for haematological malignancies but remains largely ineffective against solid tumours like CRC. Our study identifies two critical barriers to anti-CEACAM5 CAR T-cell therapy in CRC: antigen sequestration at intercellular junctions and a substantially thickened tumour cell glycocalyx. Notably, they both contribute and we cannot easily change one without changing the other in our system. By employing cutting-edge microscopy, functional analyses, cytotoxicity, and cytokine release assays, we provide mechanistic insights into CAR T-cell failure against CRC and demonstrate promising enzymatic strategies to restore therapeutic efficacy.

3.1 | Antigen Sequestration and Glycocalyx Barriers Limit CAR T-Cell Functionality

We show for the first time that CEACAM5 becomes progressively sequestered at intercellular junctions as CRC monolayers mature, rendering this target antigen increasingly inaccessible to CAR T-cells. This sequestration directly correlates with the transition from sustained to oscillatory calcium signalling in CAR T-cells and significantly decreased cytotoxicity against confluent tumour cell monolayers. CEACAM5 sequestration in CEACAM5⁺ lung cancer cell confirms its universality. The antigen-specific nature of this phenomenon is evidenced by our observation that other membrane proteins (CD19, HER2), which are successfully targeted by CAR T-cell therapy, remain homogeneously distributed and accessible regardless of monolayer maturity.

Super-resolution imaging revealed that CRC cells possess a remarkably thick glycocalyx, approximately four times thicker than that of CAR T-cells. This substantial physical barrier likely explains the delayed CAR T-cell activation kinetics observed in our experiments, as the receptor must overcome this steric hindrance to engage target antigens. The combination of antigen sequestration and glycocalyx barrier presents a formidable challenge for CAR T-cell efficacy against solid tumours.

3.2 | CD45 Exclusion Supports the Kinetic-Segregation Model in CAR T-Cell Activation

We found that CD45 exclusion is a potential mechanism of CAR T-cell activation at the anti-CEACAM5 CAR T-cell/CRC cell interface. Along with other studies, our work confirms and extends the reach of the kinetic segregation (KS) model, wherein CD45 exclusion initiates receptor triggering, to CAR T-cells at T-cell/tumour interfaces irrespective of the tumour types (liquid and solid cancer) [14, 15].

3.3 | Local and Bulk Treatments for Enzymatic Remodelling

To achieve precise intercellular dissociation without compromising the monolayer of cells to avoid glass/T-cell interaction, we employed local trypsin treatment using a micropipette (Figure 4B,C). This treatment was also used to investigate the CEACAM5 re-availability kinetics (Figure 4D and Figure S4C), ensuring same FOV before and after trypsin treatment. However, to simplify the experimental procedure, bulk treatment was employed during resPAINT measurement (Figure 4E) and experimenting with hyaluronidase (Figure 4B,C) and heparinase (Figure S4D). Our results demonstrated that both local and bulk treatments are working.

Scale bars are 10 μm . (E) 2D resPAINT image of LS-174T cell glycocalyx in presence of trypsin and corresponding line plot. Scale bar is 2 μm . Boxplot shows the comparison of glycocalyx thickness of LS-174T cell before and after trypsin treatment with $n = 20$ in each condition. (F) Violin plots show primary CAR T-cell-induced cytotoxicity (top, LDH release) and cytokine release (middle, bottom) before and after trypsin and hyaluronidase treatment on longer seeded LS-174T and LS-1034 monolayers. The medians in C, E and F were compared using two-sided Student's *t*-test. ns not significant, * $p < 0.05$, *** $p = 0.0006$, **** $p < 0.0001$.

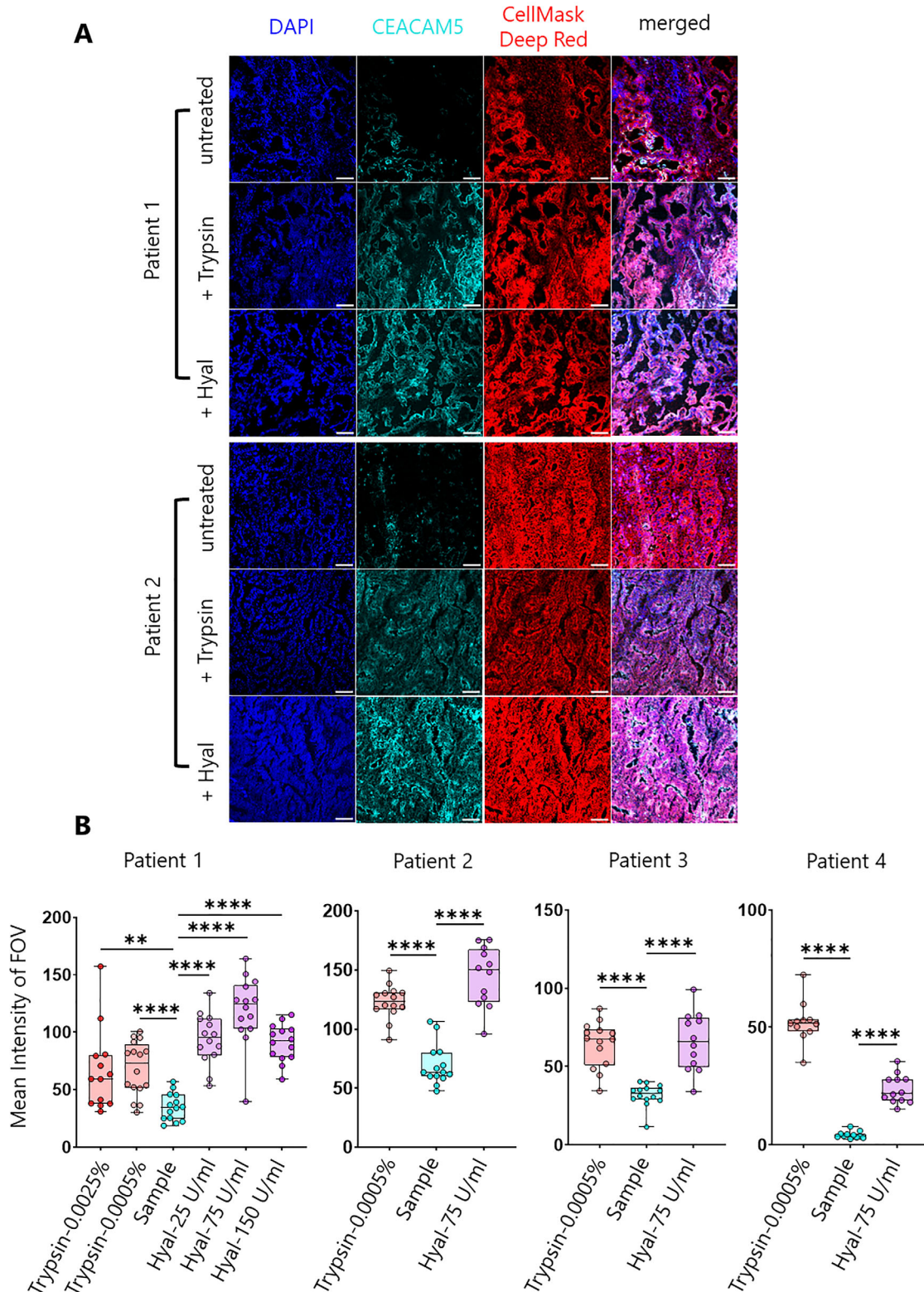


FIGURE 5 | Trypsin and hyaluronidase treatment on human colorectal cancer tissue samples. (A) Representative DAPI (blue), CEACAM5 (cyan), and CellMask Deep Red (red) and merged images from patient 1 and 2 (2 out of 4 showing significant post-treatment increase), and following trypsin (0.0005%) and hyaluronidase (75 U/mL) treatment. Scale bars are 50 μ m. (B) Boxplots show variation of mean CEACAM5 intensity in patient 1–4 tissues, and under different trypsin and hyaluronidase treatment conditions. $n = 11$ –14 FOVs were collected in each condition and each point represents a single FOV. The medians were compared using two-sided Student's t -test. ** $p = 0.0041$, **** $p < 0.0001$.

3.4 | Enzymatic Remodelling Restores CEACAM5 Accessibility and CAR T-Cell Function

Our most significant finding is that targeted enzymatic treatments effectively overcome both identified barriers. Localised trypsin application disrupted intercellular junctions, mobilised sequestered CEACAM5, and significantly reduced glycocalyx thickness. This dual mechanism of action restored sustained calcium signalling in CAR T-cells and reinstated their cytotoxic capacity against previously resistant CRC monolayers.

Importantly, hyaluronidase or heparinase treatment, which specifically targets the glycocalyx without disrupting cell-cell junctions, similarly enhanced CAR T-cell activation, suggesting that glycocalyx remodelling is a generalizable strategy to improve anti-CEACAM5 CAR T-cell efficacy. Significantly improved cytotoxicity and cytokine release following enzymatic remodelling corroborates our observation. This finding has immediate clinical relevance given hyaluronidase's established safety profile and FDA approval for other indications. The ability of three mechanistically distinct enzymes to improve CAR T-cell function provides compelling evidence that physical barriers, rather than intrinsic tumour cell resistance mechanisms, are primary impediments to CAR T-cell efficacy in CRC.

3.5 | Pre-Clinical Validation and Therapeutic Implications

Extending beyond *in vitro* models, we demonstrated that CEACAM5 is largely inaccessible in patient-derived CRC tissues, with enzymatic treatment significantly enhancing antigen detection. The differential response rates between hyaluronidase and trypsin treatment highlight tumour heterogeneity and suggest that glycocalyx remodelling may have broader applicability than junctional disruption for clinical translation. We hypothesize that CEACAM5 inaccessibility limits the efficacy of anti-CEACAM5 CAR T-cells in clinical trial [19].

3.6 | Integration with Emerging Approaches to Enhance CAR T-Cell Therapy

This work complements recent advances in solid tumour immunotherapy strategies [29–31]. While some approaches focus on enhancing CAR T-cell trafficking or persistence, our findings address the fundamental barrier of antigen accessibility at the tumour-immune interface. Our results align with studies demonstrating that disrupting tumour glycosylation enhances immunotherapy efficacy [29].

3.7 | Enzyme-Secreting CAR T Cells as a Promising Translational Strategy

Systemic administration of trypsin or hyaluronidase is clinically impractical and that engineering CAR T cells to secrete hyaluronidase represents a more translatable approach. Multiple preclinical studies have demonstrated the feasibility of this approach. Caruana et al. [31] showed that heparanase-secreting CAR T cells enhanced solid tumour infiltration without accu-

mulating in vital organs. Zhao et al. [32, 33] engineered CAR T cells to secrete human hyaluronidase PH20, enhancing tumour infiltration and suppressing growth in gastric cancer xenografts. More recently, Zhao et al. [34] developed stimulus-responsive hyaluronidase-loaded nanogels conjugated to CAR T-cell surfaces, achieving 83.2% tumour inhibition whilst minimising off-target effects.

Whilst constitutive enzyme secretion could theoretically affect CAR T-cell function, the studies above found no detrimental effects on viability or persistence. Nevertheless, we acknowledge the need for rigorous evaluation of CAR T-cell fitness, persistence, and potential toxicity before clinical translation.

Future enhancement with the spatial control afforded by localised enzymatic delivery presents advantages over systemic approaches, potentially minimizing off-target effects while maximising tumour impact. Furthermore, our findings suggest that combinatorial strategies, pairing CAR T-cells with tumour microenvironment-modifying agents, may be necessary to achieve optimal therapeutic outcomes in solid tumours.

3.8 | Validation of CEACAM5 as Target Antigen

Our findings do not invalidate CEACAM5 as a target antigen. Rather, they reveal why anti-CEACAM5 CAR T-cells have shown limited efficacy despite high tumour expression. The antigen is physically sequestered and shielded, not absent. Importantly, enzymatic remodelling restored both CEACAM5 accessibility and robust CAR T-cell killing, demonstrating that CEACAM5 remains a viable target when the glycocalyx barrier is addressed. This supports the rationale for combining anti-CEACAM5 CAR T-cells with glycocalyx-degrading strategies.

3.9 | Limitations and Future Directions

While our study provides compelling mechanistic insights, some limitations must be addressed in future work. First, the *in vitro* and *ex vivo* nature of our experiments necessitates validation in immunocompetent *in vivo* models. Second, clinical translation requires development of targeted enzyme delivery strategies to avoid systemic effects. Third, the long-term impact of glycocalyx remodelling on tumour biology requires careful evaluation. Fourth, an experiment where anti-CD19 CAR T-cells interact with CD19-expressing SLB2 (40 nm glycocalyx) and CD19⁺ LS-174T (400 nm glycocalyx) monolayer will be helpful to evaluate the effect of the glycocalyx alone on CAR T-cell triggering.

Future studies should explore the following promising directions: (1) development of enzyme-armed CAR T-cells capable of autonomously modifying their local microenvironment; (2) optimisation of hyaluronidase dosing and scheduling to maximise the therapeutic window; (3) exploration of combinatorial approaches with checkpoint inhibitors or stroma-targeting agents; (4) identification of biomarkers to stratify patients likely to benefit from this approach; (5) while our study utilised an A3-B3 domain-targeting CAR to model the overcoming of severe steric hindrance typical of membrane-proximal epitopes, future studies utilising CARs against distal epitopes (e.g., N-terminal) could further elu-

cidate how enzymatic remodelling differentially impacts binders with varying baseline accessibility; and (6) ex vivo patient explant assays or in vivo validation of the enzymatic remodelling strategy in immunocompetent tumour models would be critical next steps toward advancing this therapeutic approach to clinical trials.

4 | Conclusions

Our study reveals antigen sequestration and glycocalyx barriers as key mechanisms limiting CAR T-cell efficacy in CRC and demonstrates that enzymatic remodelling of the tumour microenvironment can effectively overcome these barriers. By elucidating these fundamental limitations and providing a rationalized approach to address them, this work establishes a framework for improving immunotherapy outcomes in colorectal cancer and potentially other solid malignancies. The use of clinically approved agents like hyaluronidase offers a pathway for rapid translation of these findings to benefit patients with currently incurable solid tumours.

5 | Methods

5.1 | Isolation and Culture of Human Primary CD8⁺ T-Cells

Fresh peripheral blood was obtained from three healthy donors after informed consent. Peripheral blood mononuclear cells (PBMCs) were enriched by density gradient centrifugation using Ficoll-Paque Plus (GE Healthcare). Naïve CD8 T-cells were isolated from PBMCs using the MagniSort Human CD8 Naïve T-cell enrichment kit according to the manufacturer's instructions (Invitrogen). One million naïve CD8⁺ T-cells were activated with plate-bound anti-CD3 (Biolegend Ultra-LEAF purified, Clone-OKT3, at 1 µg/mL) and anti-CD28 (Biolegend Ultra-LEAF purified, Clone-CD28.2, at 1 µg/mL) for 3 days. Primary CD8⁺ T-cells were cultured in Immunocult (Stem Cell Technologies) medium supplemented with 50 µg/mL of Gentamicin (Gibco) and 50 U/mL of human recombinant IL-2 (Peprotech). IL-2 was replenished after every 3 days.

5.2 | Generation of CAR T-Cells and Overexpression of Human CD19 by Sleeping Beauty (SB)

Sleeping beauty (SB) transgene cassettes were used to facilitate overexpression of human CD19 and expression of second-generation CARs targeting human CEACAM5 and CD19. All parental plasmids (pp) were designed and purchased from VectorBuilder. The CD19 SB-CAR was constructed using NEBuilder HiFi DNA Assembly Master Mix (New England Biolabs, #E2621S) according to the manufacturer's instructions. The two assembled fragments were PCR-linearized CEACAM-hMN-14 SB-CAR (with the scFv removed) and PCR-amplified anti-CD19 FMC63 single chain variable fragment (scFv) in the VL-Whitlow/218 linker-VH orientation. For CD19 overexpression in LS-174T, a puromycin resistance gene was incorporated into the transposon cassette. For anti-CEACAM5 CAR expression in primary CD8 T-cells, the hMN-14 SB vector was synthesized into a pre-clinical

TABLE 1 | Nucleofection parameters (cell number, buffer, and pulse code) for different cell types using the Lonza 4D Nucleofector.

Cell type/line	No. of cells	Buffer solution	Pulse code
Jurkat	1 million	SE	CL-120
LS-174T	1 million	SE	EN-113
Human CD8 ⁺ T-cells	2 million	P3	EO-115

grade (pGC) Gencircle (Genscript Biotech). Stable expression in cell lines was facilitated by SB100X (VectorBuilder), while SB100X mRNA (N1-Methylpseudouridine/m1Ψ) (Genscript Biotech) was employed for primary CD8⁺ T-cells. All plasmid transgene cassettes except for SB100X, which uses the CAG promoter, were under control of EF1a.

5.3 | CAR T Structure

The anti-CEACAM5 scFv comprised variable domains (VH and VL) derived from the clone hMN-14 with FMC63 being used for CD19. In contrast to anti-CD19, the CEACAM5 variable domains were linked by a poly-Glycine-Serine (G4S)₃ linker. Both CAR constructs incorporated a Strep-tag II (WSHPQFEK) sequence and a G4S2 linker, fused between the CD8α hinge and scFv domains to facilitate identification of CAR⁺ cells. The transmembrane domain from CD28 was used in conjunction with the intracellular signaling domains of CD28 and CD3ζ.

5.4 | Nucleofection and Selection of SB Delivered Cassettes

All electroporations were carried out using a Lonza 4D Nucleofector. Briefly, 1–2 million cells were resuspended in their corresponding nucleofection buffer and pulsed according to their respective code (see the following Table 1). Following nucleofection, cells were immediately rescued with 80 µL of pre-warmed complete media (antibiotic-free) and incubated at 37°C for 20 min. Subsequently, cells were further diluted and cultured in complete media. LS-174T cells were selected for CD19 expression by the addition of puromycin (1 µg/mL) (Santa-Cruz) for 1 week. Jurkat CAR⁺ cells (anti-CD19 & CEACAM5) were stained with anti-strep-tag II antibody (FITC) and enriched using the EasySep FITC Positive Selection Kit II according to the manufacturer's instructions (StemCell Technologies). Conversely, 72-h post-nucleofection CD8⁺ CAR T-cells were expanded with plate-bound CEACAM5 protein with FC tag (ACROBiosystems) at 0.5 µg/mL for 4 days in complete Immunocult media with 50 U/mL of human IL-2. The percentage of CD8⁺ CAR⁺ cells was subsequently determined by flow cytometry.

5.5 | Flow Cytometry

Flow cytometry was performed on a CytoFLEX LX Flow Cytometer, with all analysis done on FlowJo software (v10.10). Primary and CRC cell lines were stained for viability with LIVE/DEAD Fixable Near-IR and blocked with Human TruStain FcX (Biole-

gend) prior to antibody staining. For antibody staining, cells were resuspended in FACS buffer (PBS with 3% FBS). The following antibodies were used: anti-human CD8 Pacific Blue, (Biolegend, RPA-T4), The NWSHPQFEK Tag Antibody FITC, (Genscript, 5A9F9), anti-human CD19 AF594 (Biolegend, HIB19) anti-human CD340/HER-2 AF647 (Biolegend, 24D2) and anti-human CEACAM5/CD66e PE (R&D Systems, 487609). Cells were fixed in IC Fixation Buffer (eBioscience) and washed in FACS buffer twice prior to acquisition.

5.6 | Jurkat CAR T-Cell, CRC, and Lung Cancer Cell Culture

All cell lines (Jurkat, Clone E6-1, TIB-152; LS-174T, CL-188; LS-1034, CRL-2158; RKO, CRL-2577) were purchased from ATCC. The original collection source for these cell lines was the Cancer Research UK Cambridge Institute. All cell line were tested for mycoplasma and found to be negative. Jurkat CAR T-cells (CEACAM5⁺, CD19⁺), CRC cells (CEACAM5⁺ & HER2⁺ WT LS-174T, CEACAM5⁻ RKO, CD19⁺ LS-174T, CEACAM5⁺ LS-1034) and lung cancer (A549) cells were cultured in StableCell RPMI-1640 and DMEM/F-12 (1:1) (1X) + GlutaMAX-I (Dulbecco's Modifies Eagle Medium F-12 Nutrient Mixture (Ham)) medium, respectively. Both media was supplemented with 10% (v/v) fetal calf serum (FCS), 1% (v/v) HEPES buffer solution (1 M), 1% (v/v) sodium pyruvate 100 mM (100X) and 1% (v/v) pen strep antibiotics. Hereafter, we will call the supplemented media as 'complete RPMI' and 'complete DMEM.' TrypLE express enzyme was used to detach the CRC cells. Cells were then diluted and re-suspended in complete DMEM for further culture. CRC cells were passaged before they could grow confluent. All cell culture was performed in HEPA-filtered cell culture cabinets and cells were grown within the incubator with 37°C and 5% CO₂ maintaining density 0.2–0.5 million/mL. All cell lines were within 20 passage number and never continuously cultured more than 1 month.

5.7 | SLB2 Preparation and Monitoring CAR T-Cell/SLB2 Interaction Using Imaging

A mixture of 98:2 mol% POPC (Avanti Polar Lipids) and DGS-NTA-Ni²⁺ (NiNTA; Avanti Polar Lipids) was prepared as previously described for making SLB2 using the vesicle fusion technique [20]. SLB2 protein mixture presents CD58 and ICAM-1, CD45 and CD43, human CEACAM5/CD66e protein (from ACROBiosystems), and gp100-MHC. CD45 and CD43 proteins have been conjugated covalently with Alexa-555 using random lysine before use. CEACAM5 targeting Jurkat CAR T-cells were labelled with a mixture of Fluo-4-AM (calcium indicator) and Cell-Mask Deep Red Plasma Membrane Stain (ThermoFisher) before being allowed to interact with SLB2. As experimental readouts, calcium signaling, cell footprint, and close-contact (CD45/CD43 exclusion) formation were measured using a home-built microscope. Individual protein concentrations of CEACAM5⁺ and CEACAM5⁻ SLB2s are listed in Table 2.

Details of protein production, labelling, SLB2 preparation and experiments have been described in our previous publication [20].

TABLE 2 | Protein concentrations used in CEACAM5⁺ and CEACAM5⁻ supported lipid bilayers (SLB2).

	CEACAM5 ⁺ SLB2	CEACAM5 ⁻ SLB2
Protein	Conc. (ng/μL)	
CEACAM5	0.5	0
gp100-MHC	9.5	10
CD58	0.5	0.5
ICAM-1	1.2	1.2
CD45	2.5	2.5
CD43	1.5	1.5

5.8 | TIRF Microscopy

The interaction of CAR T-cell/SLB2 was imaged using a home-built microscope in total internal reflection fluorescence (TIRF) mode with three laser lines: 488 nm (200 mW, iBeam-SMART, Toptica), 561 nm (LPX-561L, LaserBoxx, Oxixius), and 641 nm (Obis, Coherent). Each laser line was attenuated by neutral density filters, expanded by a pair of plano-convex lenses, circularly polarised by a quarter-wave plate, and combined in the downstream path by appropriate dichroic mirrors. The lasers were then aligned and directed to the edge of a 100X oil-immersion objective lens (CFI Apo TIRF 100XC Oil, NA 1.49, MRD01991, Nikon), which was mounted on an inverted optical microscope (Eclipse Ti2, Nikon). Fluorescence emission was collected through the same objective lens, and a quad-band dichroic mirror (Di01-R405/488/561/635, Semrock) was used to separate the emission from the excitation light. The built-in 1.5X magnifying lens in the Ti2 microscope body was used to further improve the image resolution. Emission was then filtered through appropriate long-pass and single-band filters (BLP01-488R + FF01-520/44-25, LP02-568RS-25 + FF01-587/35-25, FF01-692/40-25; Semrock) before being collected by an EMCCD camera (Evolve 512 Delta, Photometrics). The microscope was equipped within an incubator (DigitalPixel) to maintain 37°C during live T-cell imaging. The built-in Perfect Focus System (PFS) of the TI2 microscope body was used to maintain focus during imaging, and three-colour images were acquired sequentially using Micro-Manager 2.0.0 software with a 100 ms exposure time and a 2-s interval. The pixel size of the collected images was 107 nm, measured using a line grating target (R1L3S6P, Thorlabs).

5.9 | CAR T-Cell/SLB2 Imaging Data Analysis

Data was analysed using a custom-written code described in our previous publication [20].

5.10 | CRC (WT LS-174T, LS-1034, RKO, CD19⁺ LS-174T) and Lung Cancer Cells' (A549) Monolayer Preparation

The viability of the adherent CRC and lung cancer cells was checked and counted using Countess II automated cell counter (ThermoFisher) by mixing with 1:1 trypan blue (0.4%). The cells were plated on ibidi glass bottom (35 mm, high) dish / 8-well plate

maintaining 0.3–0.6 million/mL and incubated for seeding for 24 and 48 h (early and longer, respectively).

5.11 | Calcium Imaging and Analysis

On the day of the experiment, CAR T-cells were labelled with Fluo-4-AM and allowed to interact with CRC cells' monolayer. As previously mentioned, a 488 nm laser was used for excitation, and epifluorescence calcium imaging of CAR T-cells was monitored at the T-cell/tumour interface. Imaging was performed with an exposure time of 100 ms with a 30-s interval. Initially, a 20X objective lens (Plan Fluor, NA 0.50, Nikon) was used to capture a large field of view (FOV) of T-cell/tumour interactions. Subsequently, a 60X oil-immersion objective lens (CFI Apo TIRF 60XC Oil, NA 1.49 oil-immersion, MRD01691, Nikon) was used for close inspection. The pixel size of the collected images using 20X and 60X objective lens were 800 nm and 178 nm, respectively.

Calcium imaging time-stacks were analysed using the TrackMate plugin in ImageJ/Fiji [35]. Cells within the imaging FOVs were detected and segmented using the StarDist [36] detector in TrackMate with default parameters. These segmented cells were linked into trajectories using the simple LAP tracker to capture the dynamics of a T-cell in all frames throughout the movie. Parameters for linking max distance, gap-close max distance, and gap-close max frame gap were set to ensure that segmented cells from the same cell across different frames were accurately joined. Typical parameters were 15 μm for max distances and 10 frames for max frame gap. TrackMate outputted a list of polygon regions of interest (ROI) for the segmented cells, with each ROI labelled according to the track it belonged to. The mean fluorescence intensity of each cell across all frames was measured using the Measure function in ImageJ/Fiji (Figure S5C). The results and the ROI information were saved to local files and organized using a home-written Python script, which processed the data to output intensity information as a function of time for each individual cell. Mean fluorescence intensity (I_0 indicates the first frame where T cell activity is detected; I_t denotes the subsequent frames over time) was extracted, and the ratio (I_t/I_0) was plotted as a function of time for each cell using OriginPro 2023b.

For comprehensive comparison of intensity fluctuations of Jurkat and primary CAR T-cells in triggering/non-triggering conditions, the intensity profile of each tracked cell was normalised to its maximum intensity. The variance of each profile was then computed and recorded. Violin plots were generated using GraphPad Prism 10.3.0 to visualise the distribution of intensity variations.

5.12 | CAR Accumulation Experiment

FITC-conjugated anti-strep-tag II antibody was used to label the strep-tag II of the CEACAM5⁺ Jurkat CAR T-cells and they were allowed to interact with early-seeded LS-174T monolayer. A 488 nm laser with 100 ms exposure time was used as excitation source and CAR accumulation was monitored by epifluorescence imaging with time.

5.13 | Cytotoxicity and Cytokine Release Assays

The cytotoxic activity of CEACAM5-specific CAR-T cells was evaluated using both lactate dehydrogenase (LDH) release and Annexin V/propidium iodide (PI) assays. CEACAM5^{high} LS1034 and CEACAM5^{low} LS174T colorectal cancer cell lines were cultured for 24 h to establish an early-seeded monolayer and for 48 h to form a longer-seeded monolayer. To partially dissociate cell–cell junctions and enhance CEACAM5 surface accessibility, cells were treated for 30 min with 0.0005% trypsin or 25 U/mL hyaluronidase. CEACAM5-negative RKO cells were cultured for 24 h before co-culture. Effector CEACAM5-specific CAR-T cells were co-cultured with target cells at an effector-to-target (E:T) ratio of 1:1 for 16 h. Following incubation, 50 μL of co-culture supernatant was collected for quantification of LDH release using the CytoTox 96 Non-Radioactive Cytotoxicity Assay Kit (Promega), according to the manufacturer's instructions. LDH activity in the supernatant served as a surrogate marker for target-cell lysis. After co-culture, both tumour cells and CAR-T cells were harvested and stained with Annexin V and propidium iodide to identify apoptotic tumour cells by flow cytometry. In parallel, CAR⁺CD8⁺ T cells were analysed for intracellular IFN- γ and TNF- α expression to assess effector cytokine production following CEACAM5-specific activation.

5.14 | Glycocalyx Measurement of T-Cell and LS-174T Using Super-Resolution Imaging

CAR T-cells and early-, longer-seeded LS-174T cells were fixed using a mixture of 0.8% paraformaldehyde (28906, Thermo Scientific, MA) and 0.2% glutaraldehyde (G5882, Sigma–Aldrich) at room temperature. Fixed CAR T-cells were allowed to settle on the poly-L-lysine (PLL, 150–300 kDa; P4832; Sigma–Aldrich) coated coverslip for 45 min as described in our earlier publication [24]. Sodium carbonate-bicarbonate buffer with pH 9.6 was used to dilute HMSiR conjugated wheat germ agglutinin (WGA) and used to label the glycocalyx of the cells. A 641 nm laser in highly inclined and laminated optical sheet (HILO) mode was used to excite the sample and 20 000 frames were collected with 30 ms exposure time. 2D resPAINT super-resolution imaging data was analysed in Fiji using PeakFit (GDSC SMLM 2.0) and shown in Figure 2 [27].

Diluted 0.05% Trypsin-EDTA (1X, gibco) was used for bulk treatment of early- and longer-seeded LS-174T monolayers. Trypsin-treated monolayers were washed and fixed as described before. resPAINT imaging was carried out and the results are shown in Figure 4E.

5.15 | Stimulated Emission Depletion Microscopy (STED) for LS-1034 Glycocalyx Measurement

Seeded LS-1034 cells were fixed for 20 min at room temperature as described earlier. After fixation, cells were washed three times with PBS. The glycocalyx of LS-1034 cells was labelled with Star Red (STRED-0002-1MG abberior STAR RED, NHS carbonate)-conjugated wheat germ agglutinin (WGA) for 30 min. Following labelling, cells were washed three times with PBS and prepared for imaging.

We used a commercial STED inverted microscope (Abberior STED Expert Line Super Resolution Microscope, Abberior Instruments GmbH, Göttingen, Germany). This laser scanning microscope is based on a fully automated Olympus IX83 microscope platform with a 100x (1.4 NA) oil immersion objective (UPLSAPO 100XO) and a high-precision Ultrasonic Stage (IX3-SSU). STED image acquisition was performed with pulsed 640 nm laser excitation and a depletion at 775 nm. Images were taken for a region of interest with a sampling of 20 nm. The pinhole was set to 1.0 AU. The image acquisition was controlled by Inspector software. Deconvolution was performed using Huygens Professional software (Scientific Volume Imaging, Hilversum, Netherlands) in STED mode, employing the Classic Maximum Likelihood Estimation (CMLE) algorithm.

5.16 | Antigen Mapping on LS-174T, LS-1034, and A549 Monolayer Using Antibody

PE conjugated anti-hCEACAM5 (mouse IgG_{2A}, R & D Systems), Alexa Fluor 594 conjugated anti-hCD19 (mouse IgG₁, R & D Systems) and Alexa Fluor 647 conjugated anti-human CD340 (erbB2/HER-2, Biolegend) antibodies were used for CEACAM5, CD19 and HER2 mapping, respectively. Respective lasers were used for excitation and epifluorescence images were collected.

5.17 | Granules Release Experiment and Analysis Using Imaris

Primary CAR T-cells were labelled with a mixture of Fluo-4-AM and lysotracker red (50 nM) and allowed to interact with early-seeded LS-174T monolayer. 488 and 561 nm lasers were used for excitation and epifluorescence images were collected to monitor calcium flux and granule release by CAR T-cells simultaneously (Figure 3C,D).

5.18 | Granules Release Analysis Using Imaris

Released granules from individual T-cells were tracked using Imaris 10.0.1 (Oxford Instruments). The surface function with tracking was utilized for detecting the granules. This tool allows us to create an artificial solid object (surfaces) to represent the range of interest of a specific object, like granules here. The automatic surface creation wizard in Imaris was used for segmenting granules, followed by fine-tuning the segmentation for accuracy. We used in-built tools in Imaris for this purpose, which involves adjusting the contour of the surface or correcting any segmentation errors. To make the surfaces more visible, we assigned different colours and opacity to the created surfaces. We then tracked the resulting surfaces over time using an autoregressive motion tracking algorithm. Several parameters, such as track length, track speed mean, and track straightness, were computed.

Track length: The Track Length (tl) is the total length of displacements within the Track.

Track speed mean: The mean value of the cell's speed on the track. Mean speed is determined by dividing track length by the time between the first and last object in the track.

Track straightness:

$$S = \frac{D}{L}$$

S = Track Straightness

D = Track Displacement

L = Track Length

5.19 | Segmenting and Tracking CAR T-Cells Using Imaris

Calcium imaging movies of Jurkat CAR T-cell/LS-174T interaction were monitored using 60X objective lens and used for analyzing track speed mean and track straightness of CAR T-cells using Imaris as described in previous section.

5.20 | Imaging CD45 Exclusion at T-Cell/Tumour Cell Interface Using eSPIM

5.20.1 | Optical Setup

The experiment employed an open-top single-objective light sheet microscope based on the Oblique Plane Microscopy (OPM) configuration [37]. The instrument adopted a similar design as reported by Yang et al. [38]. A primary 60X NA 1.27 water-immersion objective (CFI Plan Apo IR 60XC WI, Nikon) mounted on an inverted microscope body (Eclipse Ti-U, Nikon) was used for both light sheet launching and emission collection. Two continuous diode lasers, 488 nm (200 mW, LBX-488-200, Oxxius) and 638 nm (180 mW, 06-MLD-638, Cobolt), were expanded, collimated and combined into a single excitation path. The combined beam then passed through a cylindrical lens to generate a 1D Gaussian beam. A quad-band dichroic mirror (Di01-R406/488/561/635, Semrock) was used to separate the excitation and emission wavelengths. The beam propagated through two 4f systems before entering the primary objective at one edge of the back focal plane (BFP) to produce a 30-degree-tilted light sheet. Rapid volumetric illumination was achieved by scanning the light sheet using a 1-D Galvo mirror (GVS201, Thorlabs). The operation of the galvo mirror was controlled by a home-written LabView script.

Fluorescence collected by the primary objective was transmitted through the quad-band dichroic mirror, relayed onto a 40X secondary air objective (CFI Plan Apo Lambda D Air, NA 0.95, Nikon), with the pupil plane conjugated to that of the primary objective. Subsequently, the emission was collected by a bespoke glass-tipped tertiary objective (AMS-AGY v1.0, NA 1, Calico lab) oriented at a 30-degree angle to the optical axis. A tube lens ($F = 321$ mm) was used to direct the emission onto a sCMOS camera (Photometrics Prime 95B). Additionally, the setup featured a three-colour optical splitter (OptoSplit III, Prior) for simultaneous multi-colour imaging.

5.20.2 | Experimental Details

LS-174T and Jurkat CAR T-cells were labelled with Alexa Fluor 647 anti-human CD326 (Ep-CAM, clone 9C4, BioLegend)

antibody and Alexa Fluor 488 anti-CD45 monoclonal antibody (Gap8.3), respectively and CAR T-cells were allowed for interaction with early seeded LS-174T monolayer and incubated for 30 min to image late-stage contact formation. Volumetric scans were performed using a home-written automation script in μ Manager 2.0. During each volumetric scan, the light sheets from the 488 nm (44.4 W/cm²) and 638 nm (55.5 W/cm²) lasers scanned through the sample. The detection camera was synchronised with the galvo scanning, enabling simultaneous three-colour imaging with an exposure time of 30 ms. Each volumetric scan consisted of 100 frames (full 1200 × 1200-pixel FOV) acquired within approximately 4 s.

To monitor the late-stage dynamics at CAR T-cell/LS-174T cell interface, volumetric scans were repeated every 30 s for approximately 40–45 min. Throughout the acquisition process, the sample stage and the primary objective were enclosed within a sealed plastic chamber. The temperature around the sample was maintained at 37°C. The acquired images from each volumetric scan were deskewed and reconstructed into 3D projections using a custom Python script.

5.21 | Micropipette Preparation and Trypsin Delivery

5.21.1 | Micropipette Fabrication

Micropipettes were fabricated from borosilicate glass capillaries (World Precision Instruments, 1B150F-4), with an outer and inner diameter of 1.5 and 0.84 mm, respectively. A laser pipette puller was used for fabrication (Model P-2000, Sutter Instrument, CA) with the following parameters: (Line 1) Heat = 415, FIL = 4, VEL = 30, DEL = 200. This pulled a micropipette with a pore diameter of approximately 4–5 μ m (Figure S5D).

5.21.2 | Micropipette Delivery

The micropipette was controlled using a 3D manipulator (Scientifica PatchStar Micromanipulator, Scientifica, Uckfield, UK) to provide precise positioning of the tip above the cell. A continuous pressure pulse (0.7 psi or 5 kPa) was used to deliver trypsin, until clear disruption of the cell contacts in the second layer was observed. Careful control of the pressure pulse ensured that the cell monolayer was not disturbed in this process. A similar strategy was employed for local delivery of the fluorescent antibody.

5.22 | Hyaluronidase and Heparinase Treatment

Hyaluronidase (25 U/mL) from *Streptomyces hyalurolyticus* (Sigma, USA) and Heparinase I and III Blend (0.05, 0.5, 1.2, and 5 U/mL) from *Flavobacterium heparinum* (Merck) were used for bulk treatment on longer-seeded LS-174T monolayers for 15 and 60 min, respectively.

5.23 | Collection of human Colorectal Cancer Tissue

Human samples utilized in this research project were collected from the Imperial College Healthcare Tissue Bank (ICHTB),

which is supported by the National Institute for Health Research (NIHR) Biomedical Research Centre at Imperial College Healthcare NHS Trust and Imperial College London. The ICHTB, approved by Wales REC3 (22/WA/0214) for releasing human material for research, issued the samples under sub-collection reference numbers associated with project R24029.

5.24 | Immunofluorescence Staining of Frozen Colorectal Cancer Tissue Sections

Optimal cutting temperature (OCT)-embedded frozen human colorectal cancer samples were sectioned and mounted on glass slides. Tissue sections were treated with phosphate-buffered saline (PBS) (for untreated condition) or a specific concentration of trypsin or hyaluronidase from *Streptomyces hyalurolyticus* (Sigma, USA) for 15 min at room temperature. Following enzymatic digestion, slides were rinsed with PBS and fixed with 1% formalin solution (Sigma–Aldrich) in PBS for 10 min at room temperature. After fixation, slides were washed three times with wash buffer (PBS supplemented with 0.5% Tween-20) and permeabilized with 0.2% Triton X-100 in PBS for 10 min. This was followed by three additional washes with wash buffer. To block non-specific binding, sections were incubated with 10% goat serum (Invitrogen 31873) in wash buffer for 1 h at room temperature. Slides were then incubated overnight at 4 °C in a humidified chamber with a mouse monoclonal anti-human CEACAM5 primary antibody (CB30, S-52390; 1:500 dilution) prepared in 5% goat serum in wash buffer. The following day, slides were washed three times with wash buffer (10 min each wash at room temperature), followed by a 1-h incubation at room temperature in the dark with Alexa Fluor 488-conjugated goat anti-mouse IgG secondary antibody (Invitrogen; 1:2000 dilution in 5% goat serum in wash buffer). After secondary antibody incubation, sections were washed three times with wash buffer and counterstained with DAPI (1:2000 dilution) for 10 min. Membranes were then stained with CellMask Deep Red according to the manufacturer's protocol. Final washes were performed three times in wash buffer before slides were mounted using CitiFluor AF1 mounting medium.

5.25 | Tissue Imaging

Imaging was performed using a confocal microscope (STELLARIS8, Leica, Wetzlar, Germany). Images were acquired using a frame size of 512 × 512 pixels in the violet (405 nm excitation, 420–470 nm emission), green (488 nm excitation, 495–545 nm emission), and the far-red (637 nm excitation, 645–700 nm emission) channel. In a FOV, upper and lower Z-positions were selected based on the emission signal from the green channel (CEACAM5) and images were acquired as Z-stack with 0.5 μ m inter-stack separation.

5.26 | Tissue Imaging Analysis

The tissue image stack consists of images captured at different axial depths. To quantify the level of exposed CEACAM5 before and after trypsin treatment, we compared the mean intensity of the FOV before and after treatment. Image analysis was

performed in Fiji/ImageJ. Each Z-stack was first processed using a maximum intensity Z-projection to generate a single representative image of the entire FOV. The resulting projection was then converted to 8-bit, and an intensity threshold of 20–255 was applied. The mean intensity of the FOV was measured using the ‘Measure’ function in ImageJ and recorded. The same analysis and intensity threshold were consistently applied to images from all patient samples. Multiple FOVs across 13 patient samples were analysed. The mean FOV intensity before and after trypsin treatment was visualised using box plots for each patient sample.

5.27 | Statistical Analysis

Experimental data were presented as violin or box plots with individual data points indicating independent measurements. Violin and box plots display the median and quartile ranges. CAR expression data were reported as the mean \pm standard deviation (SD). Statistical analysis was performed using Graphpad Prism 10.3.0. Two-sided paired and unpaired Student’s *t*-test were performed as required for statistical significance in Figures 1–5 and Figures S2–S5. Sample size (*n*) and probability (*p*) values were reported in the individual figure legends.

5.28 | Data and Code Availability

All imaging data needed to evaluate the conclusion are present in the paper and the supplementary materials and movies. Codes are available in Github (https://github.com/mkoerbel/contactanalysis_2D, <https://github.com/Zui409>, and <https://github.com/Zui409/Intensity-tracking/tree/main>). All additional datasets of the current study are available from the corresponding authors on request.

Author Contributions

Conceptualization: D.B. and D.K. Methodology: D.B., P.S., B.L., D.H., S.K., Z.Z., S.J.D., B.M., and D.K. Cells and reagents provided: C.J.W., J.P.R., M.A.C., S.J.D., and B.M. Investigation: D.B., C.J.W., S.C., P.S., B.L., D.H., J.P., and B.M. Visualization: D.B., C.J.W., S.K., and Z.Z. Funding acquisition: D.B., B.M., S.J.D., and D.K. Project administration: D.B., B.M., and D.K. Supervision: B.M. and D.K. Writing – original draft: D.B. and D.K. Writing – review & editing: D.B., S.J.D., B.M., and D.K.

Acknowledgements

We gratefully acknowledge the flow cytometry facility from the School of Biological Sciences for their support and assistance, and Cambridge Advanced Imaging Centre (CAIC) for providing access to their data analysis workstation and software. Additionally, we would also like to give thanks to Genscript Biotech for kindly providing pre-clinical grade Gencircles and SB100X mRNA (N1-Methylpseudouridine/m1Ψ). STED imaging was performed using the STED microscope funded by BBSRC grant BB/R000395/1 at the Department of Genetics, School of Biological Sciences, University of Cambridge. Deconvolution was performed using the Light Microscopy Core Facility at Cancer Research UK Cambridge Institute.

Funding

This work was supported by Horizon Europe Marie Skłodowska-Curie Actions (MSCA) guarantee grant award (Project no. MBAG/773,

Award no. G114341) provided by the UK Research and Innovation (UKRI), and Cancer Research UK (CRUK) grant (award reference DRCCIPA\100010). B.M. is supported by CRUK Career Development Fellowship (RCCFEL\100095), NSF-BIO/UKRI-BBSRC project grant (BB/V006126/1), and MRC project grant (MR/V028995/1).

Conflicts of Interest

The authors declare no conflict of interest.

Data Availability Statement

The data that support the findings of this study are available from the corresponding author upon reasonable request.

References

1. G. Gross, T. Waks, and Z. Eshhar, “Expression of Immunoglobulin-T-Cell Receptor Chimeric Molecules as Functional Receptors with Antibody-Type Specificity,” *Proceedings of the National Academy of Sciences* 86, no. 24 (1989): 10024–10028, <https://doi.org/10.1073/pnas.86.24.10024>.
2. C. H. June, R. S. O’Connor, O. U. Kawalekar, S. Ghassemi, and M. C. Milone, “CAR T Cell Immunotherapy for human Cancer,” *Science* 359, no. 6382 (2018): 1361–1365, <https://doi.org/10.1126/science.aar6711>.
3. D. L. Porter, B. L. Levine, M. Kalos, A. Bagg, and C. H. June, “Chimeric Antigen Receptor–Modified T Cells in Chronic Lymphoid Leukemia,” *New England Journal of Medicine* 365, no. 8 (2011): 725–733, <https://doi.org/10.1056/NEJMoal103849>.
4. J. H. Park, I. Rivière, M. Gonen, et al., “Long-Term Follow-Up of CD19 CAR Therapy in Acute Lymphoblastic Leukemia,” *New England Journal of Medicine* 378 (2018): 449–459, <https://doi.org/10.1056/NEJMoal709919>.
5. G. Guzman, M. R. Reed, K. Bielamowicz, B. Koss, and A. Rodriguez, “CAR-T Therapies in Solid Tumors: Opportunities and Challenges,” *Current Oncology Reports* 25, no. 5 (2023): 479–489, <https://doi.org/10.1007/s11912-023-01380-x>.
6. S. M. Albelda, “CAR T Cell Therapy for Patients with Solid Tumours: Key Lessons to Learn and Unlearn,” *Nature Reviews Clinical Oncology* 21 (2024): 47–66, <https://doi.org/10.1038/s41571-023-00832-4>.
7. X. Qin, F. Wu, C. Chen, and Q. Li, “Recent Advances in CAR-T Cells Therapy for Colorectal Cancer,” *Frontiers in Immunology* 13 (2022): 904137, <https://doi.org/10.3389/fimmu.2022.904137>.
8. B. Ghazi, A. E. Ghanmi, S. Kandoussi, A. Ghouzlani, and A. Badou, “CAR T-Cells for Colorectal Cancer Immunotherapy: Ready to Go?,” *Frontiers in Immunology* 13 (2022): 978195, <https://doi.org/10.3389/fimmu.2022.978195>.
9. J. Weng, S. Li, Z. Zhu, et al., “Exploring Immunotherapy in Colorectal Cancer,” *Journal of Hematology & Oncology* 15 (2022): 95, <https://doi.org/10.1186/s13045-022-01294-4>.
10. D. C. Harrer, S.-S. Li, M. Kaljanac, M. Barden, H. Pan, and H. Abken, “Fine-Tuning the Antigen Sensitivity of CAR T Cells: Emerging Strategies and Current Challenges,” *Frontiers in Immunology* 14 (2023): 1321596, <https://doi.org/10.3389/fimmu.2023.1321596>.
11. L. Wu, J. Brzostek, P. D. Sakthi Vale, et al., “CD28-CAR-T Cell Activation Through FYN Kinase Signaling Rather Than LCK Enhances Therapeutic Performance,” *Cell Reports Medicine* 4 (2023): 100917, <https://doi.org/10.1016/j.xcrim.2023.100917>.
12. J. H. Esensten, Y. A. Helou, G. Chopra, A. Weiss, and J. A. Bluestone, “CD28 Costimulation: From Mechanism to Therapy,” *Immunity* 44, no. 5 (2016): 973–988, <https://doi.org/10.1016/j.immuni.2016.04.020>.
13. A. J. Davenport, R. S. Cross, K. A. Watson, et al., “Chimeric Antigen Receptor T Cells Form Nonclassical and Potent Immune Synapses Driving Rapid Cytotoxicity,” *Proceedings of the National Academy of Sciences* 115, no. 9 (2018): E2068–E2076, <https://doi.org/10.1073/pnas.1716266115>.

14. Q. Xiao, X. Zhang, L. Tu, J. Cao, C. S. Hinrichs, and X. Su, "Size-Dependent Activation of CAR-T Cells," *Science Immunology* 7 (2022): abl3995, <https://doi.org/10.1126/sciimmunol.abl3995>.
15. S. J. Davis and P. A. van der Merwe, "The Kinetic-Segregation Model: TCR Triggering and Beyond," *Nature Immunology* 7 (2006): 803–809, <https://doi.org/10.1038/ni1369>.
16. C. Zhang, L. Wang, Q. Zhang, et al., "Screening and Characterization of the scFv for Chimeric Antigen Receptor T Cells Targeting CEA-Positive Carcinoma," *Frontiers in Immunology* 14 (2023): 1182409, <https://doi.org/10.3389/fimmu.2023.1182409>.
17. D.-S. Baek, Y.-J. Kim, S. Vergara, et al., "A Highly-Specific Fully-Human Antibody and CAR-T Cells Targeting CD66e/CEACAM5 are Cytotoxic for CD66e-Expressing Cancer Cells *In Vitro* and *In Vivo*," *Cancer Letters* 525 (2022): 97–107, <https://doi.org/10.1016/j.canlet.2021.10.041>.
18. Y.-J. Kim, W. Li, D. V. Zhelev, J. W. Mellors, D. S. Dimitrov, and D.-S. Baek, "Chimeric Antigen Receptor-T Cells are Effective Against CEACAM5 Expressing Non-Small Cell Lung Cancer Cells Resistant to Antibody-Drug Conjugates," *Frontiers in Oncology* 13 (2023): 1124039, <https://doi.org/10.3389/fonc.2023.1124039>.
19. F. C. Thistlethwaite, D. E. Gilham, R. D. Guest, et al., "The Clinical Efficacy of First-Generation Carcinoembryonic Antigen (CEACAM5)-Specific CAR T Cells is Limited by Poor Persistence and Transient Pre-Conditioning-Dependent Respiratory Toxicity," *Cancer Immunology, Immunotherapy* 66, no. 11 (2017): 1425–1436, <https://doi.org/10.1007/s00262-017-2034-7>.
20. E. Jenkins, M. Körbel, C. O'Brien-Ball, et al., "Antigen Discrimination by T Cells Relies on Size-Constrained Microvillar Contact," *Nature Communications* 14 (2023): 1611, <https://doi.org/10.1038/s41467-023-36855-9>.
21. R. M. Sharkey, et al., "Evaluation of a Complementarity-Determining Region-Grafted (Humanized) Anti-Carcinoembryonic Antigen Monoclonal Antibody in Preclinical and Clinical Studies," *Cancer Research* 55 (1995): 5935–5945.
22. J. M. Jessup, "Adhesion to Carcinoembryonic Antigen by Human Colorectal Carcinoma Cells Involves at Least Two Epitopes," *International Journal of Cancer* 55 (1993): 262–268, <https://doi.org/10.1002/ijc.2910550216>.
23. R. A. Morgan, J. C. Yang, M. Kitano, M. E. Dudley, C. M. Laurencot, and S. A. Rosenberg, "Case Report of a Serious Adverse Event Following the Administration of T Cells Transduced with a Chimeric Antigen Receptor Recognizing ERBB2," *Molecular Therapy* 18, no. 4 (2010): 843–851, <https://doi.org/10.1038/mt.2010.24>.
24. L. Möckl, "The Emerging Role of the Mammalian Glycocalyx in Functional Membrane Organization and Immune System Regulation," *Frontiers in Cell and Developmental Biology* 8 (2020): 253.
25. L. Möckl, P. Pedram, A. R. Roy, et al., "Quantitative Super-Resolution Microscopy of the Mammalian Glycocalyx," *Developmental Cell* 50 (2019): 57–72.
26. S. Park, M. J. Colville, J. H. Paek, et al., "Immunoengineering can Overcome the Glycocalyx Armour of Cancer Cells," *Nature Materials* 23 (2024): 429–438, <https://doi.org/10.1038/s41563-024-01808-0>.
27. E. W. Sanders, A. R. Carr, E. Bruggeman, et al., "resPAINT: Accelerating Volumetric Super-Resolution Localisation Microscopy by Active Control of Probe Emission," *Angewandte Chemie International Edition* 61 (2022): 2022069, <https://doi.org/10.1002/anie.202206919>.
28. Y. Zeng, E. E. Ebong, B. M. Fu, and J. M. Tarbell, "The Structural Stability of the Endothelial Glycocalyx After Enzymatic Removal of Glycosaminoglycans," *PLoS One* 7, no. 8 (2012): 43168, <https://doi.org/10.1371/journal.pone.0043168>.
29. B. Greco, V. Malacarne, F. De Girardi, et al., "Disrupting N-Glycan Expression on Tumor Cells Boosts Chimeric Antigen Receptor T Cell Efficacy Against Solid Malignancies," *Science Translational Medicine* 14 (2022): abg3072, <https://doi.org/10.1126/scitranslmed.abg3072>.
30. Y. Wu, Y. Liu, Z. Huang, et al., "Control of the Activity of CAR-T Cells Within Tumours via Focused Ultrasound," *Nature Biomedical Engineering* 5, no. 11 (2021): 1336–1347, <https://doi.org/10.1038/s41551-021-00779-w>.
31. I. Caruana, B. Savoldo, V. Hoyos, et al., "Heparanase Promotes Tumor Infiltration and Antitumor Activity of CAR-Redirected T Lymphocytes," *Nature Medicine* 21 (2015): 524–529, <https://doi.org/10.1038/nm.3833>.
32. R. Zhao, Y. Cui, Y. Zheng, et al., "Human Hyaluronidase PH20 Potentiates the Antitumor Activities of Mesothelin-Specific CAR-T Cells Against Gastric Cancer," *Frontiers in Immunology* 12 (2021): 660488, <https://doi.org/10.3389/fimmu.2021.660488>.
33. Y. Zhao, Y. Dong, S. Yang, et al., "Bioorthogonal Equipping CAR-T Cells with Hyaluronidase and Checkpoint Blocking Antibody for Enhanced Solid Tumor Immunotherapy," *ACS Central Science* 8 (2022): 603–614, <https://doi.org/10.1021/acscentsci.2c00163>.
34. H. Zhao, Y. Gao, S. Ma, et al., "Hyaluronidase Nanogel-Armed CAR-T Cell for Synergistically Reducing Tumor Extracellular Matrix and Improving Efficacy Against Solid Tumors," *Nano Research* 18 (2025): 94907359, <https://doi.org/10.26599/NR.2025.94907359>.
35. D. Ershov, M.-S. Phan, J. W. Pylvänäinen, et al., "TrackMate 7: Integrating State-of-the-Art Segmentation Algorithms Into Tracking Pipelines," *Nature Methods* 19 (2022): 829–832, <https://doi.org/10.1038/s41592-022-01507-1>.
36. U. Schmidt, M. Weigert, C. Broaddus, and G. Myers, "Cell Detection with Star-Convex Polygons," *Medical Image Computing and Computer Assisted Intervention—MICCAI 2018* (Springer, 2018), 265–273.
37. C. Dunsby, "Optically Sectioned Imaging by Oblique Plane Microscopy," *Optics Express* 16, no. 25 (2008): 20306–20316, <https://doi.org/10.1364/OE.16.020306>.
38. B. Yang, X. Chen, Y. Wang, et al., "Epi-Illumination SPIM for Volumetric Imaging with High Spatial-Temporal Resolution," *Nature Methods* 16, no. 6 (2019): 501–504, <https://doi.org/10.1038/s41592-019-0401-3>.

Supporting Information

Additional supporting information can be found online in the Supporting Information section.

Supporting File 1: advs73422-sup-0001-SuppMat.docx.

Supporting File 2: advs73422-sup-0002-MovieS1.mp4.

Supporting File 3: advs73422-sup-0003-MovieS2.mp4.

Supporting File 4: advs73422-sup-0004-MovieS3.mp4.

Supporting File 5: advs73422-sup-0005-MovieS4.mp4.

Supporting File 6: advs73422-sup-0006-MovieS5.mp4.

Supporting File 7: advs73422-sup-0007-MovieS6.mp4.

Supporting File 8: advs73422-sup-0008-MovieS7.mp4.

Supporting File 9: advs73422-sup-0009-MovieS8.mp4.

Supporting File 10: advs73422-sup-0010-MovieS9.mp4.

Supporting File 11: advs73422-sup-0011-MovieS10.mp4.

Supporting File 12: advs73422-sup-0012-MovieS11.mp4.

Supporting File 13: advs73422-sup-0013-MovieS12.mp4.

Supporting File 14: advs73422-sup-0014-MovieS13.mp4.

Supporting File 15: advs73422-sup-0015-MovieS14.mp4.

Supporting File 16: advs73422-sup-0016-MovieS15.mp4.